

# Reconstructing Images from Projections Using the Maximum-Entropy Method. Numerical Simulations of Low-Aspect Astrotomography

A. T. Bajkova

*Main Astronomical Observatory, Russian Academy of Sciences, St.Petersburg, 196140 Russia*

Received February 2, 2007; in final form, April 5, 2007

**Abstract** — The reconstruction of images from a small number of projections using the maximum-entropy method (MEM) with the Shannon entropy is considered. MEM provides higher-quality image reconstruction for sources with extended components than the Högbom CLEAN method, which is also used in low-aspect astrotomography. The quality of image reconstruction for sources with mixed structure containing bright, compact features embedded in a comparatively weak, extended base can be further improved using a difference-mapping method, which requires a generalization of MEM for the reconstruction of sign-variable functions. We draw conclusions based on the results of numerical simulations for a number of model radio sources with various morphologies.

PACS numbers : 95.75.Mn, 95.75.Pq, 98.70.Dk, 98.54.Gr

DOI: 10.1134/S1063772907110030

## 1. INTRODUCTION

The reconstruction of images from projections (reconstructive tomography) is of interest in many fields, from medicine to astronomy [1]. Examples in astronomy include reconstructing the brightness distributions of astrophysical objects from lunar-occultation observations [2–4] and Doppler-tomography analysis of binary star systems [5–8]. The synthesis of images using radar methods is also of considerable interest [9, 10].

The problem of reconstructing images using nonlinear algorithms possessing high interpolating and extrapolating properties arises when the number of projections is small (low-aspect astrotomography), and there are large unfilled regions (“holes”) in the data plane. In such cases, the use of linear methods, such as reverse filtered projections [1], becomes inexpedient due to the impossibility of reconstructing the missing spectral information and the poor quality of the resulting images [11].

One class of image-reconstruction methods is based on the radio-astronomy approach [11–13], using the well known CLEAN algorithm of Högbom [14] or its modification [15]. In this case, the observational data (projections) are used to form a “dirty” image, which is the convolution of the desired distribution and the synthesized beam. As a result, the task of reconstructing an image reduces to solving for the inverse convolution, which is an ill-posed problem.

Agafonov and Podvoiskaya [11, 12] propose solving this problem as is traditionally done in aperture synthesis. In particular, they use an algorithm with two CLEAN procedures in order to obtain two solutions, one of which better represents the compact and the other the extended features in the source structure [12]. The first solution is obtained by applying a standard Högbom CLEAN, and the second using the modified CLEAN algorithm proposed in [15] for reconstructing images of extended sources. However, methods that are able to reconstruct all of the structural components of a source equally accurately, thus yielding a more objective representation of its structure, are of greater interest. One such alternative image-reconstruction method is the maximum-entropy method (MEM), using the Shannon entropy [16, 17], which is also well known in low-aspect astrotomography [5–7].

The absence of any *a priori* restrictions on the source structure (except for the assumption that it is finite in extent) makes MEM a more fundamental method than the CLEAN method initially proposed for the reconstruction of point-like sources. Another advantage of MEM over both the standard and modified [15] CLEAN methods is its independence of a number of specified parameters, whose choice appreciably influences the quality of the reconstruction.

The aim of the current work is to investigate the possibilities of MEM in the reconstruction of

images with various types of morphologies when the number of available projections of the data is very limited. We also consider ways to improve MEM to make it more suitable for the reconstruction of images consisting of bright, compact features embedded in a weaker, extended base. To solve this latter problem, we propose a difference maximum-entropy method, whose realization requires a generalization of the standard MEM algorithm to the case of reconstructing sign-variable functions.

In the following sections of the paper, we present a mathematical formulation of low-aspect astrotomography, describe the process of reconstruction from data projections, describe the maximum-entropy method (both its generalized form and the difference method), and carry out a comparative analysis of the results of numerical simulations of image reconstruction.

## 2. FORMULATION OF THE PROBLEM

The problem we consider here can be formulated as follows. Let us consider a two-dimensional source of radiation having a finite spatial extent on the sky in the region  $(X, Y)$ . Such an object is described mathematically by a two-dimensional, finite, non-negative function of the variables  $X$  and  $Y$ ,  $O(X, Y)$  (Fig. 1a). The projection of the object onto a line  $p$  making an angle  $\phi$  with the  $Y$  axis, as is shown in Fig. 1a, is the integral of the intensity distribution in the object over the coordinate perpendicular to the direction of  $p$ . The projection is a function of the variable  $p$ , which we denote  $T(p)$ . Let there be  $N$  projections of the object at different angles  $\phi_i$ , so that there are  $N$  integrals  $T_i(p)$  ( $i = 1, \dots, N$ ) for the two-dimensional object along directions comprising angles  $\phi_i + 90^\circ$  with the  $Y$  axis. Our task is to reconstruct the image  $O(X, Y)$  from the projections  $T_i(p)$ .

## 3. RECONSTRUCTION FROM PROJECTIONS

At the basis of the algorithm we used to reconstruct images from projections lies the fundamental relation between the Radon transform and the Fourier transform, formulated as a projection theorem [1]: the Fourier transform of a projection  $T(p)$  at an angle  $\phi$  to the  $Y$  axis (Fig. 1a) is the one-dimensional central cross section of the two-dimensional Fourier transform of the function  $O(X, Y)$  at the same angle  $\phi$  to the  $V$  axis in the spatial-frequency domain  $(U, V)$  (the  $UV$  plane). Figure 1b shows the  $(U, V)$  coordinates of the Fourier transform of the projection  $T(p)$ . An example with six projections, which we used for our simulations, is illustrated in Fig. 2a, and the corresponding coverage of the  $UV$  plane is shown in Fig. 2b. If the number of projections is infinite, the reconstruction of the image

is obtained via an inverse Radon transform [1].

Note that the fundamental possibility of reconstructing an image from a small number of projections, or equivalently with incomplete coverage of the  $UV$  spatial-frequency domain, is based on the property that the Fourier transform of the finite function describing the spatially finite object is analytic [18]. Analytic functions can be extended throughout an infinite space in which they are defined using the known values in a finite interval or at a finite set of points.

The main requirement for a reconstruction algorithm is non-linearity. Only due to this non-linearity is it possible to realize the “analytic continuation” of a spectrum; i.e., to fill empty regions (“holes”) in the  $UV$  plane [17]. It is fundamentally impossible to obtain the missing spectral harmonics using linear procedures. In many cases, the requirement that the solution be non-negative turns linear procedures into appreciably non-linear ones (for example, in the least-squares method). In the standard MEM approach, non-negativity is an intrinsic internal property of the solution, indicating the appreciable non-linearity of the method.

## 4. THE MAXIMUM-ENTROPY METHOD

MEM is one of a large class of non-linear informational methods [19] whose essence lies in the optimization of a functional specified by some informational criterion for the quality of the solution (the maximum information, entropy,  $\alpha$ -divergence, etc.), subject to the fulfillment of various linear or nonlinear constraints that flow from the data [17]. In our case, maximizing the Shannon entropy consists in finding the maximum of the functional

$$E = \int x(t) \ln(1/x(t)) dt = - \int x(t) \ln(x(t)) dt, \quad (1)$$

where  $x(t)$  is the desired distribution and, in accordance with the projection theorem, measurements of the spatial Fourier spectrum of the source serve as the data to be used, leading to linear constraints in the form of equalities.

Since the numerical simulations suppose working with digital data, we present a discrete formulation of the optimization. Let a map of an object with a finite carrier be discretized in accordance with the Shannon–Kotel’nikov theorem and have a size of  $N \times N$  pixels. We denote the discrete measurements of the desired distribution

$$x_{kl}, \quad k, l = 1, \dots, N - 1.$$

We denote the known measurements of the two-dimensional Fourier spectrum of the object, which represent the data, in accordance with the projection

theorem, as follows, separating the real,  $A_m$ , and imaginary,  $B_m$ , parts:

$$X_m = A_m + jB_m, \quad m = 1, \dots, M,$$

where  $M$  is the number of known measurements and  $m$  is the number of the current measurement with coordinates  $(u_m, v_m)$  in the  $UV$  plane, not necessarily located at nodes of the coordinate grid. This last circumstance means that there is no problem with pixelization of the data in the frequency domain, which represents a certain technical advantage of this method over other methods [1] and appreciably enhances the accuracy of the reconstruction.

The practical MEM algorithm we applied, taking into account the errors in the data [17, 20], supposes the solution of the conditional-optimization problem

$$\min \sum_k \sum_l x_{kl} \ln(x_{kl}) + \rho \sum_m \frac{(\eta_m^{re})^2 + (\eta_m^{im})^2}{\sigma_m^2}, \quad (2)$$

$$\sum_k \sum_l x_{kl} a_{kl}^m - \eta_m^{re} = A_m, \quad (3)$$

$$\sum_k \sum_l x_{kl} b_{kl}^m - \eta_m^{im} = B_m, \quad (4)$$

$$x_{kl} \geq 0, \quad (5)$$

where  $a_{kl}^m$  and  $b_{kl}^m$  are constant coefficients (cosines and sines) that flow from the Fourier transform,  $A_m$  and  $B_m$  are the real and imaginary parts of the spectral data for the object,  $\eta_m^{re}$  and  $\eta_m^{im}$  are the real and imaginary parts of the instrumental additive noise, which has a normal distribution with zero mean and known dispersions  $\sigma_m$ , and  $\rho$  is a positive weight.

As we can see from (2), the optimized functional has two parts: a Shannon-entropy functional and a functional that is an estimate of the difference between the reconstructed spectrum and the measured data according to a  $\chi^2$  criterion. This latter functional can be considered an additional regulating, or stabilizing, term acting to provide a further regularization of the solution above that possible with the entropy functional alone [20]. The influence of this additional term on the resolution of the reconstruction algorithm must be borne in mind [7].

Equations (3)–(4) represent linear constraints on the unknown images  $x_{kl}$  and noise terms  $\eta_m^{re}$  and  $\eta_m^{im}$ . The non-negativity constraint on the image (5) can be omitted in this case due to the nature of the entropy solution, which is purely positive.

Note that, due to the fact that there is always a zero point in the  $UV$  plane (the total flux of the source  $F_0$ ), this automatically brings about the normalization of the solution required for MEM:

$$\sum_k \sum_l x_{kl} = F_0.$$

The numerical algorithm for the reconstruction (2)–(5) treating this as a non-linear optimization problem based on the Lagrange-multiplier method, is considered in detail in [19]. Here, we present only the solution:

$$x_{kl} = \exp\left(-\sum_m (\alpha_m a_{kl}^m + \beta_m b_{kl}^m) - 1\right), \quad (6)$$

$$\eta_m^{re} = \frac{\sigma_m^2 \alpha_m}{\rho}, \quad \eta_m^{im} = \frac{\sigma_m^2 \beta_m}{\rho}, \quad (7)$$

expressed in terms of the Lagrange multipliers (dual variables)  $\alpha_m$  and  $\beta_m$ , through which the constraints (3) and (4), respectively, enter the Lagrange functional.

As we can see from (6), the standard MEM image is manifestly positive. It is not difficult to show that the MEM Hesse matrixes everywhere positive definite, so that the entropy functional is convex and the solution is global.

Various gradient methods can be used to search for the extrema of the corresponding dual functional. We used a coordinate-descent method, since it is the most reliable means to search for the global solution.

## 5. GENERALIZED MAXIMUM-ENTROPY METHOD

The realization of the difference-mapping principle described in Section 6 requires a generalized MEM algorithm for the reconstruction of arbitrary real functions that take on both positive and negative values. We adopt the following definition of the entropy of such an arbitrary real function.

**Definition 1.** The entropy  $E$  of an arbitrary real function  $x(t)$  that can, in general, take on both positive and negative values is defined as the entropy of the modulus of this function,  $|x(t)|$  [20]:

$$E = - \int |x(t)| \ln(|x(t)|) dt. \quad (8)$$

We denote the positive part of the function  $x(t)$  as  $x^p(t)$ , and its negative part  $-x^n(t)$ , with both  $x^p(t)$  and  $x^n(t)$  being non-negative:  $x^p(t), x^n(t) \geq 0$ . The function  $x(t)$  can then be represented in the form

$$x(t) = x^p(t) - x^n(t), \quad (9)$$

with  $x(t)$  being determined by only one of these terms at each value  $t$  — either  $x^p(t)$  or  $x^n(t)$ ; in this case, we can define the modulus of the function

$$x(t) = x^p(t) \quad \text{если} \quad x(t) \geq 0, \quad (10)$$

$$x(t) = -x^n(t) \quad \text{если} \quad x(t) < 0.$$

Obviously, the relation

$$x^p(t) \cdot x^n(t) = 0 \quad (11)$$

is equivalent to the conditions (10). When the conditions (10) are fulfilled, expression (8) takes the standard form

$$E = - \int x^p(t) \ln(x^p(t)) + x^n(t) \ln(x^n(t)) dt.$$

Let us also define the associated entropy [20].

**Definition 2.** The associated entropy of the function  $x(t)$  is given by the expression

$$E(\alpha) = - \int x(t) \ln(\alpha x(t)) dt, \quad (12)$$

where  $\alpha$  is a real, positive parameter. The associated entropy (12) differs from the usual entropy (1) in the presence of  $\alpha$  in the logarithm.

Let us now define the generalized entropy of a real, sign-variable function.

**Definition 3.** The generalized entropy of a real, sign-variable function (9) is its associated entropy, calculated as follows:

$$E(\alpha) = - \int (x^p(t) \ln(\alpha x^p(t)) + x^n(t) \ln(\alpha x^n(t))) dt. \quad (13)$$

In this case, the parameter  $\alpha$  plays a leading role, since its value determines the accuracy with which the positive and negative parts of the solution  $x(t)$  can be separated, and thus the quality of the reconstructed image.

Let us consider this further. Omitting all intermediate steps, we write the solution for the corresponding discrete optimization problem (13) in terms of the dual variables:

$$\begin{aligned} x_{kl}^p &= \exp(-\sum_m (\alpha_m a_{kl}^m + \beta_m b_{kl}^m) - 1 - \ln \alpha), \\ x_{kl}^n &= \exp(\sum_m (\alpha_m a_{kl}^m + \beta_m b_{kl}^m) - 1 - \ln \alpha), \end{aligned} \quad (14)$$

whence it follows that the series  $x_{kl}^p$  and  $x_{kl}^n$  are related by an expression that depends only on  $\alpha$ :

$$x_{kl}^p \cdot x_{kl}^n = \exp(-2 - 2 \ln \alpha) = K(\alpha). \quad (15)$$

As we can see from (15),  $\alpha$  indeed plays the role of an agent separating the positive and negative parts of the solution (14). We can achieve any specified accuracy with which the conditions (10) and (11) are to be satisfied by varying  $\alpha$ , since  $K(\alpha) \rightarrow 0$  as  $\alpha \rightarrow \infty$ . However, we note that the value of  $\alpha$  is bounded from above by purely computational effects. In our simulations,  $\alpha$  was specified to be 1000. When the noise is taken into account as is done in (2)–(4), the solution (7) also appears.

## 6. DIFFERENCE-MAPPING METHOD

The difference-mapping method is based on the fundamental linearity of the Fourier transform. Bright

components in the source that are reconstructed in the first stage are subtracted from the input spectrum, the remaining reconstruction is carried out for the residual spectral data, and the results of the two reconstructions are finally summed.

In the following section, we show that, when MEM – a method with clearly expressed non-linear properties – is used for the reconstruction, the difference-mapping method can lead to an appreciable improvement in the quality of the resulting image, especially when the source has both compact features and a fairly weak extended base. This type of source structure is most problematic from the point of view of the accuracy with which all the structural components are reconstructed. The reconstruction of uniform structures – either purely compact or purely extended – is much simpler (see also Section 7).

What is the reason for this improvement in the quality of the reconstruction? After subtracting from the input spectral data bright components reconstructed by MEM in the first stage, we obtain a residual spectrum in which the weak, extended component comprises a high proportion compared to the compact component. (We will call the result of this subtraction the first-order residual spectrum.) In this way, we have artificially lowered the dynamic range and increased the structural uniformity of the map corresponding to the residual spectrum, thereby facilitating the accurate reconstruction of the image in the second stage of the procedure.

If we subtract from the residual spectrum bright components in the image reconstructed in the second stage, we will obtain a second-order residual spectrum, which will correspond to a map with still lower dynamic range and higher structural uniformity. Continuing in this way, we can obtain residual functions of the spectrum of higher and higher order. To obtain the desired map of the source, we must sum the map reconstructed in the final stage with all the components subtracted from the input spectrum in previous stages.

Formally, the two-stage difference-mapping algorithm can be represented

$$F_{sp}^1 = F_{sp}^0 - F_{sp}^{br1},$$

where  $F_{sp}^0$  are the input data for the spectrum of the desired brightness distribution over the source  $x(t)$ ,  $F_{sp}^{br1}$  is the spectrum corresponding to the bright components reconstructed in the first stage  $x(t)_{br1}$ , and  $F_{sp}^1$  is the first-order residual spectrum corresponding to the map of the source reconstructed in the second stage  $x(t)_2$ . The resulting map will have the form

$$x(t) = x(t)_{br1} + x(t)_2.$$

Let us now note an important property of the difference mapping. The residual spectral data obtained after subtracting bright components reconstructed in previous stages of the algorithm

can correspond to an image with negative values. This can occur if early bright components are reconstructed with overestimated amplitudes, as is quite probable for any non-linear method. To avoid undesirable nonlinear distortions of the maps, we must carry out the reconstruction using the MEM algorithm generalized for functions that can take both positive and negative values, described in Section 5.

## 7. RESULTS OF THE NUMERICAL SIMULATIONS

We present here the results of our numerical simulations of low-aspect astrotomography for six model sources with various morphologies, denoted *1* to *6* (Fig. 3). Source *1* is a set of three resolved, compact Gaussian features; source *2* a set of three unresolved, extended Gaussian features; source *3* a combination of extended and compact Gaussian features; and sources *4*, *5*, and *6* close double sources with a weak, extended background. Sources *4*, *5*, and *6* have different intensities for the extended base emission (in *4*, it comprises 30% of the maximum amplitude of the components, and in *5* and *6*, only 10%) and different ratios for the amplitudes of the compact features (in *4* and *5*, the amplitude ratio is 1.0 : 0.8, and in *6*, 1.0 : 0.3).

We obtained input data for each numerical image reconstruction simulation using six projections at angles  $\phi_1 = 0^\circ$ ,  $\phi_2 = 90^\circ$ ,  $\phi_3 = 45^\circ$ ,  $\phi_4 = 135^\circ$ ,  $\phi_5 = 63.5^\circ$ ,  $\phi_6 = 116.5^\circ$ . The arrangement of these projections in the image plane is shown in Fig. 2a, where the numbers denote the projection numbers. The synthesized coverage of the *UV* spatial frequency plane derived using the projection theorem is shown in Fig. 2b. A modest amount of instrumental noise having a normal distribution with a zero mean was added to the artificial data, such that the signal-to-noise ratio for all examples was about ten, as is typical for astronomical observations of this type.

The aim of the simulations was to investigate capabilities of the developed algorithms in reconstructing images of sources with various structures. This is most interesting from the point of view of the preferred use of some specific reconstruction algorithm in some specific situation.

All the model sources shown in Fig. 3 are finite, and their spectra are analytic, indicating the fundamental possibility of reconstructing their images using an incomplete set of spectral data. A small (insignificant) disruption of the analyticity condition arose due to the addition of a modest amount of noise to the artificial data. However, as was established in the course of the simulations, small variations in the data lead to small variations in the solutions, indicating the stability of the developed algorithms against noise.

The images were reconstructed from the projections using the standard MEM algorithm, the generalized

difference MEM procedure, and the Högbom CLEAN algorithm, to enable comparison of the proposed algorithms with an algorithm traditionally used in radio astronomical data analysis [11-13].

The results of reconstructing sources *1-6* are presented in Figs. 4-9; panels (a) show the dirty images, corresponding to the real coverage of the *UV* plane (Fig. 2b), calculated as the inverse Fourier transform of the spectral-data measurements; panels (b) the images reconstructed using the standard CLEAN method with loop gain  $\gamma = 0.1$ ; panels (c) the images reconstructed using the standard MEM algorithm; and panels (d) the images reconstructed using the difference-mapping method with the generalized MEM. In all the images, the minimum contour and the steps between the contours are 2.5% of the peak value.

Our analysis of these images shows that the quality of the reconstruction depends substantially on the structure of the object. Let us consider the MEM maps (maps (c) in Figs. 4-9). The highest-quality reconstruction was obtained for uniform sources, consisting purely of either compact or extended features (sources *1* and *2*). In these cases, we obtain a nearly exact reconstruction (the errors in the reconstruction are no more than 3% and no more than 1% respectively). The reconstruction is worse for sources comprised of a set of extended and compact features (sources *3-6*; the maximum errors are about 10% for source *3* and, on average, 20% for sources *4-6*). The higher the dynamic range of the map, the lower the quality of the reconstruction, especially for the extended part of the structure. We were not able to accurately reconstruct the extended structures in sources *4-6*, and we can see that their outlines repeat the fan-like pattern of the *UV* coverage; this demonstrates that it was not possible to adequately interpolate the spectral data between the sections shown in Fig. 2b. Moreover, the quality of the reconstruction becomes worse the weaker the extended base in the source structure. In this case, the difference mapping method comes to the rescue. As we can see from maps (d) in Figs. 4-9, the largest improvement from the difference-mapping method is obtained for compact structures embedded in a weak, extended base (sources *4-6*). This method was able to reconstruct both the compact and extended features with high accuracy. The quantitative characteristics of the reconstructed maps show that applying the difference method makes it possible to increase the signal-to-noise ratio and decrease the maximum discrepancy between the true and reconstructed images by, on average, a factor of three; the effect of applying the difference method becomes greater the weaker the extended base in the source structure.

Let us now turn to the CLEAN maps. The images in panels (b) in Figs. 4-9 show that the best reconstruction of the source shape occurs for

the compact structures (source 1). However, even in this case, CLEAN was not able to reconstruct the amplitude ratios as accurately as MEM: the least compact source is most stretched in amplitude, and is narrowed in space (the maximum error in the reconstruction was 30%). In the case of a purely extended structure (source 2), the solution corresponds to a patchy image, although the general shape of the object was reproduced reasonably well (the maximum error was about 20%). The worst reconstruction was obtained for source 3, with a mixed structure. The reconstructed amplitude ratios for the point-like components were distorted (the maximum error was about 45%). The extended part of the structure was also appreciably distorted, and the area of the extended base was substantially decreased, leading to large distortions in the general shape of the object. We observe the same behavior for sources 4–6. Here, compact features were reproduced better by the standard MEM (on average, by 14%), but there were large spatial distortions in the reconstruction of the extended base, and we observe a substantial narrowing of this base, which becomes more prominent the weaker its intensity.

Thus, these results of our numerical simulations show that the MEM algorithm is preferable to the traditional CLEAN algorithm, especially from the point of view of accurately reconstructing extended source structures. In the case of purely compact sources, the use of CLEAN is quite justified, especially given the quick operation of this algorithm. Application of the difference-mapping method is expedient for sources containing both compact and comparatively weak extended features, when accurate reconstruction of all components of the structure is required.

Obviously, the comparative analysis of the various methods we have presented here is far from complete; in particular, we have not considered the modified CLEAN algorithm of [15], designed for the reconstruction of extended sources. However, the comparison of the standard and modified CLEAN algorithms presented in [12] shows that the standard CLEAN is best able to reconstruct compact sources, and the modified CLEAN extended sources. Therefore, in the case of complex, mixed structures, it was proposed to use a two-CLEAN method to obtain the entire range of possible solutions. We have proposed such a MEM algorithm based on a difference approach that enables the reconstruction of both extended and compact structures in an object with equal accuracy, demonstrating its advantages over both the standard and the modified CLEAN algorithms.

## 8. CONCLUSION

Due to the validity of the projection theorem, the application of MEM provides a completely natural and

simple solution for the reconstruction of images from a small number of projections.

The results of our comparison of the developed reconstruction methods based on MEM with the standard CLEAN method demonstrate the advantages of the former, since they provide a higher quality reconstruction of extended features. This is due to the fact that the MEM solutions are smooth, while the standard CLEAN algorithm operates in a space of  $\delta$ -functions, leading to discontinuous solutions. The application of a standard CLEAN algorithm is justified for compact structures, since it provides a sufficiently high quality reconstruction and rapid operation in this case.

The most difficult task is the reconstruction of images with mixed structures containing bright, compact and weaker extended features. For this case, we have proposed and studied a difference mapping method based on the MEM algorithm generalized for the reconstruction of sign-variable functions. Our numerical simulations show that this difference-mapping method is able to appreciably increase the accuracy of the reconstruction of both extended and compact features, compared to the traditional MEM algorithm. A comparison of our simulation results with the results of [12] indicate that the MEM difference-mapping method is preferable to both the standard CLEAN algorithm and the modified CLEAN algorithm of [12], designed for the reconstruction of images of extended sources.

Moreover, the generalized MEM algorithm for the reconstruction of sign - variable (and also complex) functions [20] makes it possible to substantially expand the range of practical application of this algorithm for the reconstruction of various physical signals.

We note also that there is no problem with the pixelization of data in the frequency domain in the case of MEM, which is a technical advantage that appreciably influences the accuracy of the reconstructions that can be obtained [1].

## 9. ACKNOWLEDGMENTS

The author thanks the referee for valuable comments that led to improvement of this article.

## REFERENCES

1. G. Hermen, *Image Reconstruction from Projections* (Academic, New York, 1980; Mir, Moscow, 1983).
2. S. Hoener, *Astrophys. J.* **140**, 65 (1964).
3. F. P. Maloney and S. T. Gottesman, *Astrophys. J.* **234**, 485 (1979).
4. M. I. Agafonov, V. P. Ivanov, and O. A. Podvoiskaya, *Astron. Zh.* **67**, 549 (1990) [*Sov. Astron.* **34**, 275

(1990)].

5. T. R. Marsh and K. Horne, Mon. Not. R. Astron. Soc. **235**, 269 (1988).

6. T. R. Marsh and K. Horne, Astrophys. J., **364**, 637 (1990).

7. T. R. Marsh, astro-ph/0011020 v1 (2000).

8. M. I. Agafonov, O. I. Sharova, and M. T. Richards, Preprint No 505, NIRFI (Radiophysical Research Institute, Nizhnii Novgorod State University, Nizhnii Novgorod, 2006).

9. A. F. Kononov, Zarub. Radioelektron. No 1, 35 (1991).

10. V. I. Koshelev, S. E. Shipilov, and V. P. Yakubov, Radiotekh. Elektron. **44**, 301 (1999) [J. Commun. Technol. Electron. **44**, 281 (1999)].

11. M. I. Agafonov and O. A. Podvoiskaya, Izv. Vyssh. Uchebn. Zaved., Radiofiz. **32**, 742 (1989).

12. M. I. Agafonov and O. A. Podvoiskaya, Izv. Vyssh. Uchebn. Zaved., Radiofiz. **33**, 1185 (1990).

13. M. I. Agafonov and O. I. Sharova, Izv. Vyssh. Uchebn. Zaved., Radiofiz. **48**, 367 (2005).

14. J. A. Högbom, Astron. Astrophys., Suppl. Ser. **15**, 417 (1974).

15. D. G. Steer, P. E. Dewdney, and M. R. Ito, Astron. Astrophys. **137**, 159 (1984).

16. B. R. Frieden, J. Opt. Soc. Am. **62**, 511 (1972).

17. R. Narayan and R. Nityananda, Ann. Rev. Astron. Astrophys. **24**, 127 (1986).

18. Ya. I. Khurgin and V. P. Yakovlev, *Finite Functions in Physics and Engineering* (Nauka, Moscow, 1971) [in Russian].

19. A. T. Bajkova, Soobshch. Inst. Prikl. Astron., No 58 (IPA RAN, St. Petersburg, 1993).

20. B. R. Frieden and A. T. Bajkova, Appl. Opt. **33**, 219 (1994).

*Translated by D. Gabuzda*

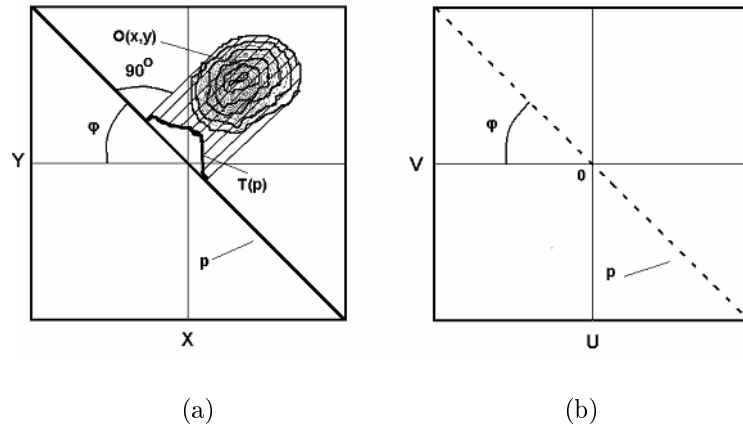


**Fig. 1.** Graphical illustration of the theory of projections: (a) region in which the object is defined ( $X, Y$ ); (b) region of spatial frequencies of the object ( $U, V$ ).

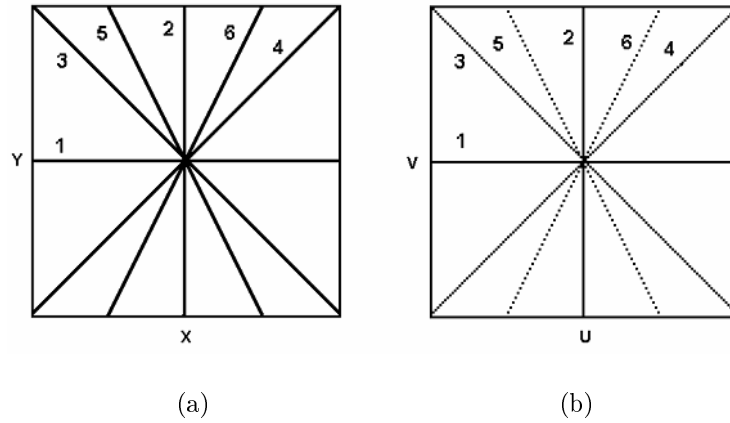


**Fig. 2.** Example of six projections: (a) geometry of the projections in the region of the object ( $X, Y$ ); (b) corresponding coverage of the spatial-frequency domain for the object ( $U, V$ ). The numbers denote the numbers of the projections.

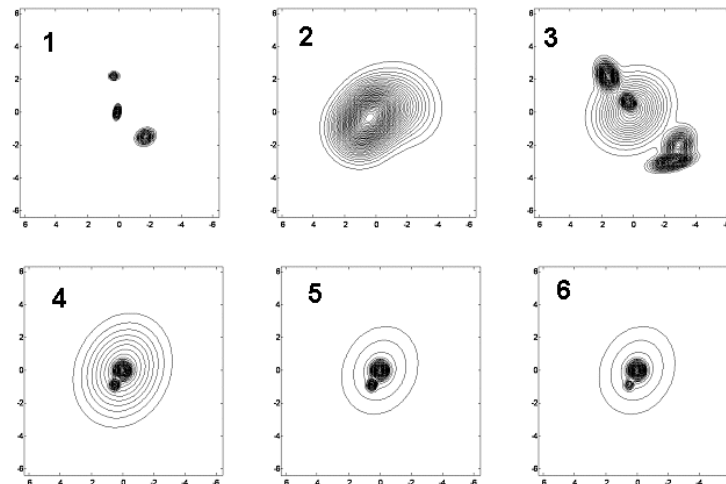


**Fig. 3.** Images of model radio sources with various morphological types. The numbers 1–6 denote the source number.

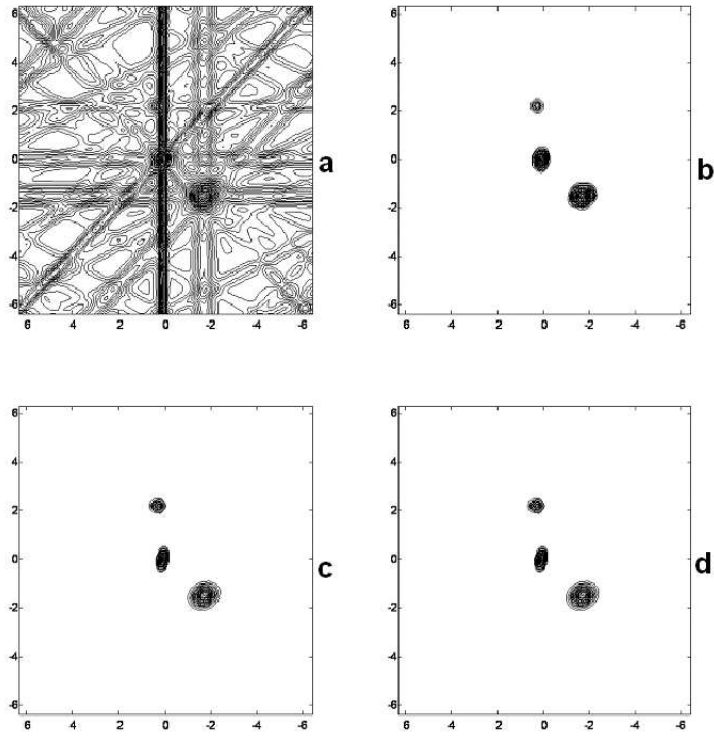


**Fig. 4.** Results of reconstructing radio source 1: (a) the dirty image, (b) the CLEAN image, (c) the MEM image and (d) the image obtained using the difference generalized MEM algorithm.

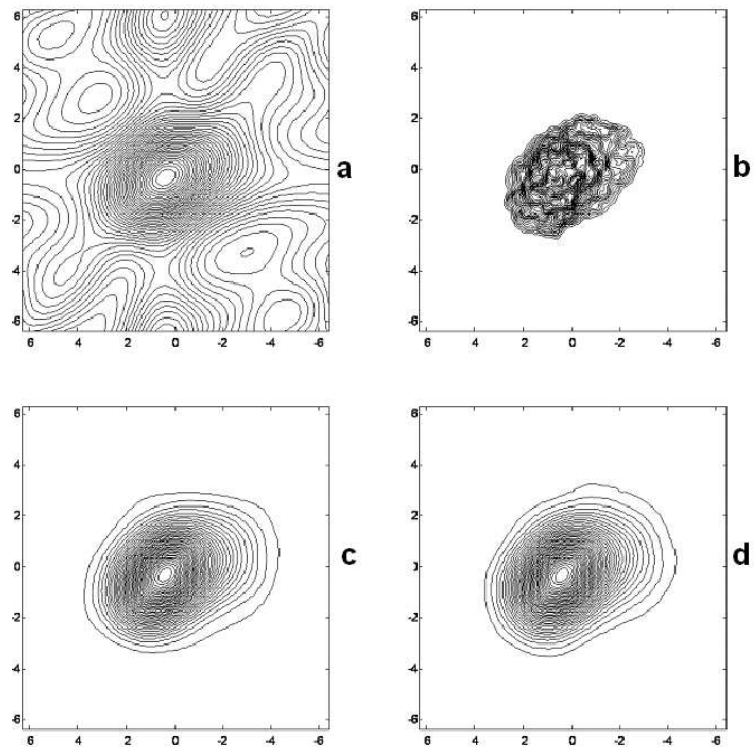


**Fig. 5.** Same as Fig. 4 for radio source 2.

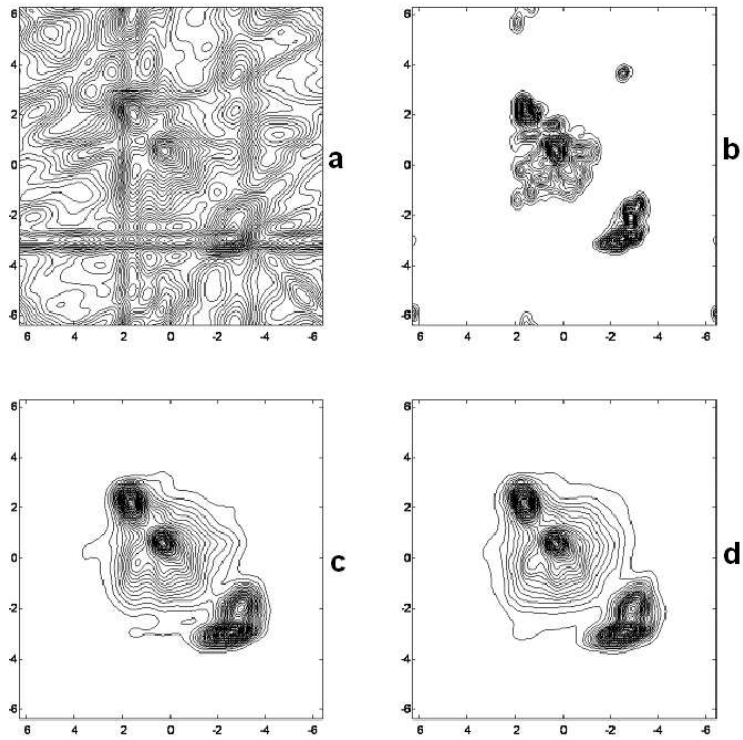


**Fig. 6.** Same as Fig. 4 for radio source 3.

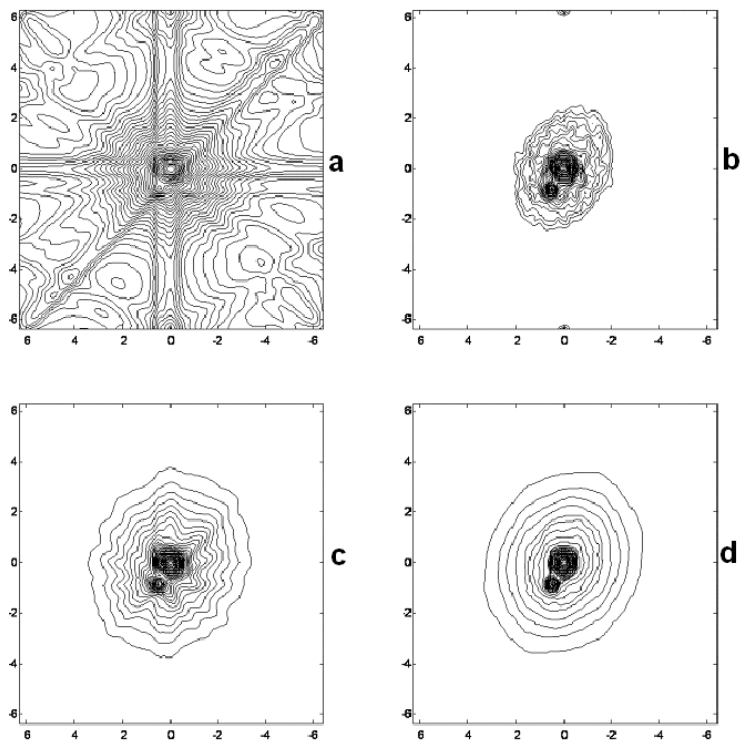


**Fig. 7.** Same as Fig. 4 for radio source 4.

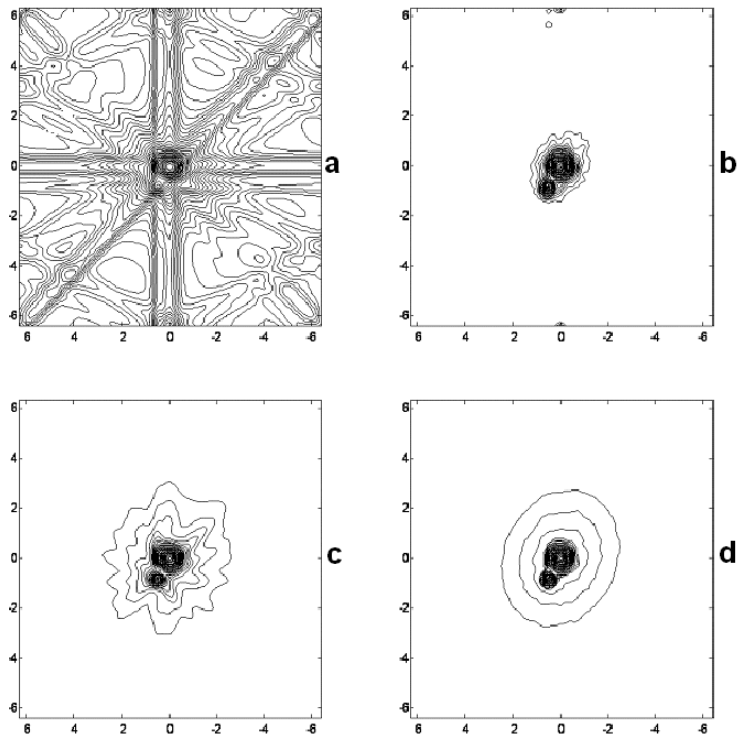


**Fig. 8.** Same as Fig. 4 for radio source 5.

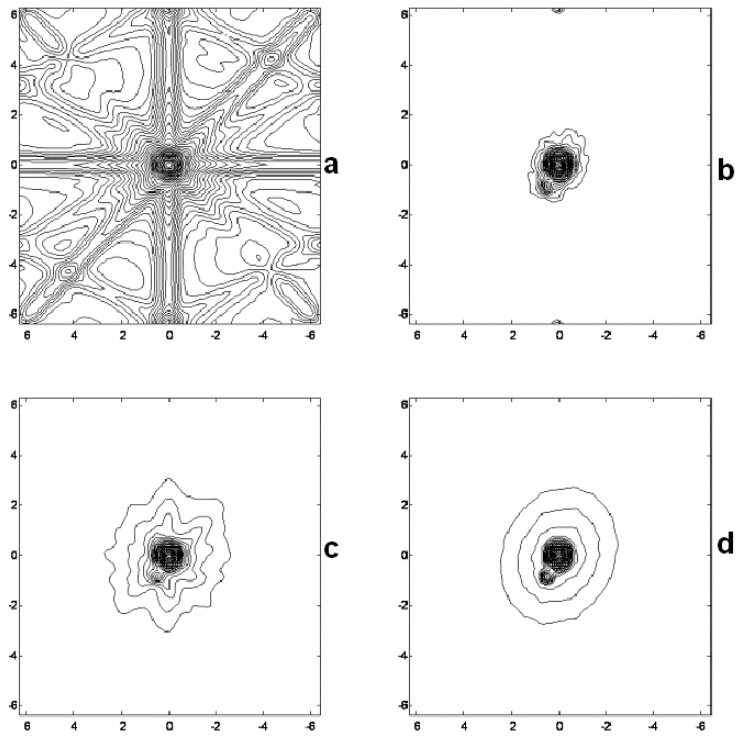


**Fig. 9.** Same as Fig. 4 for radio source 6.